



HAL
open science

Spline driven: high accuracy projectors for 3D tomographic reconstruction from few projections

Fabien Momey, Éric Thiébaud, Catherine Burnier-Menessier, Loïc Denis, Jean-Marie Becker, Laurent Desbat

► To cite this version:

Fabien Momey, Éric Thiébaud, Catherine Burnier-Menessier, Loïc Denis, Jean-Marie Becker, et al.. Spline driven: high accuracy projectors for 3D tomographic reconstruction from few projections. 2014. hal-00990015v1

HAL Id: hal-00990015

<https://hal.science/hal-00990015v1>

Preprint submitted on 12 May 2014 (v1), last revised 5 Aug 2015 (v2)

HAL is a multi-disciplinary open access archive for the deposit and dissemination of scientific research documents, whether they are published or not. The documents may come from teaching and research institutions in France or abroad, or from public or private research centers.

L'archive ouverte pluridisciplinaire **HAL**, est destinée au dépôt et à la diffusion de documents scientifiques de niveau recherche, publiés ou non, émanant des établissements d'enseignement et de recherche français ou étrangers, des laboratoires publics ou privés.

Spline driven: high accuracy projectors for 3D tomographic reconstruction from few projections

Fabien Momey*, Éric Thiébaud, Catherine Burnier, Loïc Denis, Jean-Marie Becker, and Laurent Desbat

Abstract—Tomographic iterative reconstruction methods need a very thorough modeling of data. The core of this issue is the projectors’s design, i.e. the numerical model of projection, is mostly influenced by the representation of the object of interest, decomposed on a basis of functions, and on the approximations made for the projection on the detector.

Voxel driven and *ray driven* projection models, widely appreciated for their short execution time, are too coarse. *Distance driven* model has a better accuracy but also relies on strong approximations to project voxel basis functions. Cubic voxel basis functions are anisotropic, modeling accurately their projection is therefore computationally expensive. Smoother and more isotropic basis functions both better represent continuous functions and provide simpler projectors. This consideration has led to the development of spherically symmetric volume elements, called blobs. Set apart their isotropy, blobs are often considered too computationally expensive in practice.

We propose to use 3D B-splines, which are smooth piecewise polynomials, as basis functions. When the degree of these polynomials increases, their isotropy improves and projections can be computed regardless of their orientation. Thanks to their separability, very efficient algorithms can be used to decompose an image on B-spline basis functions. We approximate the projection of B-spline basis functions with a 2D separable model. The degree and the sampling of the B-splines can be chosen according to a tradeoff between approximation quality and computational complexity.

We show on numerical experiments that with our accurate projector, the number of projections can be reduced while preserving a similar reconstruction quality. Used with cubic B-splines, our projector requires just twice as many operations as a model involving voxel basis functions. High accuracy projectors

can enhance the resolution of existing systems, or can reduce the number of projections required to reach a given resolution, potentially reducing the dose absorbed by the patient.

Index Terms—Tomography, Reconstruction, Inverse Problems, Signal processing, B-splines.

EDICS: COI-TOM - Tomographic Imaging.

I. INTRODUCTION

ITERATIVE reconstruction methods for tomography have long proven their ability to enhance reconstruction quality, compared to the filtered backprojection (FBP) [2]. The drawback of iterative methods is their expensive computation time. Due to very low signal-to-noise ratio in PET/SPECT imaging, iterative methods are preferred because they yield better results as they can use a more realistic model of the underlying physics and counting statistic of positron annihilations. However FBP [7] is still the method of choice in X-ray computed tomography. Nevertheless ongoing researches on algorithms and recent enhancements in computational power, such as multi-core processor units or GPU-based implementation facilities, call for a re-evaluation of the potential of iterative reconstruction in this domain.

Such methods require a numerical model of the data acquisition process: the so-called *projector*. It is used for the reprojection of the current estimate of the object to be reconstructed. These projections are then compared with the actual data at each iteration step. A backprojection operator is also needed, which is the adjoint of the projector. In order to fully exploit the data, the projector has to accurately model the physical process of data acquisition (X-ray transform) while being as fast as possible.

II. TOMOGRAPHIC PROJECTORS FOR ITERATIVE RECONSTRUCTION

A. The direct model

The object of interest is the starting point of the projector used in iterative reconstruction. Let $f : \mathbf{x} \mapsto f(\mathbf{x})$ be the 3D function modeling the volume to be reconstructed and defined for all space coordinates $\mathbf{x} = (x, y, z) \in \mathbb{R}^3$. The function $f(\mathbf{x})$ is directly related to the attenuation of the X-rays by the object of interest (SI units: m^{-1}) and the observed intensity $I(\mathbf{u})$ follows from the physical principle of the Beer-Lambert law:

$$I(\mathbf{u}) = I_0 \exp\left(-\int_{\mathbf{x} \in L(\mathbf{u})} f(\mathbf{x}) d\mathbf{x}\right) \quad (1)$$

with I_0 the intensity of the X-ray source and $L(\mathbf{u})$ the straight line from the X-ray source S to the position \mathbf{u} on the detector.

This work was supported by the MiTiV project (Méthodes Inverses pour le Traitement en Imagerie du Vivant), funded by the French ANR (N° ANR-09-EMER-008).

Fabien Momey* was with the Université de Lyon, F-42023, Saint-Etienne, France; CNRS, UMR5516, Laboratoire Hubert Curien, F-42000, Saint-Etienne, France; Université de Saint-Etienne, Jean Monnet, F-42000, Saint-Etienne, France. He was also with the Université de Lyon, Lyon, F-69003, France; Université Lyon 1, Observatoire de Lyon, 9 avenue Charles André, Saint-Genis Laval, F-69230, France; CNRS, UMR 5574, Centre de Recherche Astrophysique de Lyon; École Normale Supérieure de Lyon, Lyon, F-69007, France. He is now with the Université Grenoble Alpes, F-38000 Grenoble, France; CEA, LETI, MINATEC Campus, F-38054 Grenoble, France (e-mail: fabien.momey@cea.fr).

Éric Thiébaud is with the Université de Lyon, Lyon, F-69003, France; Université Lyon 1, Observatoire de Lyon, 9 avenue Charles André, Saint-Genis Laval, F-69230, France; CNRS, UMR 5574, Centre de Recherche Astrophysique de Lyon; École Normale Supérieure de Lyon, Lyon, F-69007, France (e-mail: eric.thiebaud@univ-lyon1.fr).

Loïc Denis, Catherine Burnier and Jean-Marie Becker are with the Université de Lyon, F-42023, Saint-Etienne, France; CNRS, UMR5516, Laboratoire Hubert Curien, F-42000, Saint-Etienne, France; Université de Saint-Etienne, Jean Monnet, F-42000, Saint-Etienne, France (e-mail: loic.denis,catherine.burnier,jean-marie.becker@univ-st-etienne.fr).

Laurent Desbat is with the Université Grenoble Alpes, TIMC-IMAG, F-38000 Grenoble, France; CNRS, TIMC-IMAG, F-38000 Grenoble, France; CHU de Grenoble, TIMC-IMAG, F-38000 Grenoble, France (e-mail: laurent.desbat@imag.fr).

A convenient parametric model of the object of interest consists in approximating $f(\mathbf{x})$ by a decomposition on a shift-invariant basis of functions $\varphi_k(\mathbf{x}) = \varphi(\mathbf{x} - \mathbf{x}_k)$:

$$f(\mathbf{x}) \approx \tilde{f}(\mathbf{x}) = \sum_k c_k \varphi(\mathbf{x} - \mathbf{x}_k) \quad (2)$$

where $\varphi(\mathbf{x})$ is the kernel function of the basis and the 3D positions $\mathbf{x}_k = (x_k, y_k, z_k)^T \in \mathbb{R}^3$ define a regularly spaced grid of N samples. The approximation $\tilde{f}(\mathbf{x})$ of $f(\mathbf{x})$ in (2) is a 3D function characterized by the N -dimensional vector of coefficients:

$$\mathbf{c} = (c_1, c_2, \dots, c_N)^T \in \mathbb{R}^N. \quad (3)$$

The sampled object $f_k = \tilde{f}(\mathbf{x}_k)$ (required for display and analysis) can be computed from the coefficients:

$$\mathbf{f} = \Phi \cdot \mathbf{c} \quad (4)$$

where $\Phi_{k,k'} = \varphi(\mathbf{x}_k - \mathbf{x}_{k'})$ showing that the interpolation by Φ is essentially a discrete convolution.

The projection of the object f for a given orientation of the tomographic system (positions of the source and the detector relative to the volume of interest), denoted by θ , is given by:

$$\tilde{y}^\theta(\mathbf{u}) = \int_{\mathbf{x} \in L^\theta(\mathbf{u})} f(\mathbf{x}) \, d\mathbf{x} = \sum_k c_k F_k^\theta(\mathbf{u}), \quad (5)$$

where

$$F_k^\theta(\mathbf{u}) = \int_{\mathbf{x} \in L^\theta(\mathbf{u})} \varphi(\mathbf{x} - \mathbf{x}_k) \, d\mathbf{x}, \quad (6)$$

is the so-called footprint of the k -th basis function. As a result the projector can be written as:

$$\tilde{\mathbf{y}}^\theta = \mathbf{R}^\theta \cdot \mathbf{c} \quad \text{with} \quad R_{qk}^\theta = F_k^\theta(\mathbf{u}_q), \quad (7)$$

where $\tilde{\mathbf{y}}^\theta$ gathers the data model values $\tilde{y}_q^\theta = \tilde{y}^\theta(\mathbf{u}_q)$ at the position \mathbf{u}_q of the q -th detector pixel.

B. Regularized reconstruction

The reconstruction amounts to seeking the coefficients \mathbf{c} which minimize a criterion with the general form [19], [2]:

$$\begin{aligned} \mathbf{c}^+ &= \arg \min_{\mathbf{c}} \sum_{\theta} \mathcal{J}_{\text{data}}^\theta(\tilde{\mathbf{y}}^\theta | \mathbf{y}^\theta) + \mu \mathcal{J}_{\text{prior}}(\mathbf{f}) \\ &= \arg \min_{\mathbf{c}} \sum_{\theta} \mathcal{J}_{\text{data}}^\theta(\mathbf{R}^\theta \cdot \mathbf{c} | \mathbf{y}^\theta) + \mu \mathcal{J}_{\text{prior}}(\Phi \cdot \mathbf{c}). \end{aligned} \quad (8)$$

In this criterion, $\mathcal{J}_{\text{data}}^\theta$ is a data-fidelity term which ensures consistency of the model $\tilde{\mathbf{y}}^\theta$ with the data \mathbf{y}^θ . The term $\mathcal{J}_{\text{prior}}$ accounts for prior information and is needed to regularize the inverse problem and avoid noise and artifacts amplifications. The hyperparameter μ controls the tradeoff between data fitting and regularity. Having a fast projector is critical because the minimization is performed with iterative methods.

C. State-of-the-art in tomographic projection

The choice of the basis function $\varphi(\mathbf{x})$ and the approximations made to compute its footprints $F_k^\theta(\mathbf{u})$ are essential for an accurate and fast modeling of the projections. A list of desirable properties of basis functions are:

- i. Accurate modeling of the object $f(\mathbf{x})$ that preserves important object features such as sharp edges.
- ii. Compact support for $\varphi(\mathbf{x})$ to ensure the sparsity of the resulting projector.
- iii. Separability along spatial dimensions to reduce the computational burden by factorizing computations.
- iv. Robustness to geometric transformations of the object (translation, rotation, magnification).
- v. Spherical symmetry for isotropic projection.

Standard models such as *voxel driven* or *ray driven* [5] are based on raw samples which are linearly interpolated (either in the object space or in the data space) for the purpose of the projection. The coarse approximations made by such models give rise to strong artifacts in the reconstructed object unless a great deal of projections are used (typically several hundreds) to smooth out the consequences of the approximations.

Most existing models use cubic voxels as their basis functions. These functions are advantageous for being easy to manipulate and very compact as a given voxel does not spread over its neighbors. The *distance driven* projector [1] is based on such basis functions. This model projects the voxel's central section that is mostly parallel to the detector plane. Then the obtained quadrilateral footprint is approximated with a rectangle covering at best the delimited region. The overlapping areas on the impinged detector pixels are used to weight the voxel value, and thus calculate the contribution of the voxel to each pixel. Long *et al.* [3] proposed a much more accurate projection of a cubic voxel given by a separable footprint composed of trapezoidal functions. Their model is exact in parallel beam geometry.

The anisotropic behavior of cubic voxels contrasts with the isotropic nature of tomographic projection. The choice of isotropic basis functions has led to so-called "blobs" [8], [9], [10], [11], [12], improving the accuracy of the models of the object and its projections. In tomography, the Kaiser-Bessel function is a main representative of this class of functions. Ziegler *et al.* [25] developed a blob-based projector by pre-computing the 2D footprint once for all.

III. THE SPLINE DRIVEN PROJECTOR

A. Modeling the object

1) *Approximation error:* Given the basis of functions, the best coefficients c_k should minimize some measure $\|f - \tilde{f}\|$ of the approximation error. In sampling theory [23], $\|f - \tilde{f}\|$ is usually the L_2 norm and the optimal \tilde{f} is thus the orthogonal projection of f on the subspace spanned by the basis functions φ_k . The least approximation error ϵ_f only depends on the kernel function φ , on the sampling step Δ and, of course, on the object $f(\mathbf{x})$. In 1D, an expression of the least error is [22]:

$$\epsilon_f = \min_{\mathbf{c}} \|f - \tilde{f}\|_2 \approx \left[\int_{-\infty}^{+\infty} E_\varphi(\omega\Delta) |\hat{f}(\omega)|^2 \frac{d\omega}{2\pi} \right]^{1/2} \quad (9)$$

where the hat denotes the Fourier transform and E_φ is the error kernel defined by:

$$E_\varphi(\omega) = 1 - \frac{|\hat{\varphi}(\omega)|^2}{\sum_{k \in \mathbb{Z}} |\hat{\varphi}(\omega + 2k\pi)|^2}. \quad (10)$$

For a given sampling step, a good basis function should have a low least approximation error ϵ_f .

2) *B-splines as basis functions*: Splines of degree d are piecewise polynomial functions with degree at most d and continuously differentiable up to order $d - 1$. Splines on a regular grid of samples can be written as a unique linear combination of a regularly shifted kernel. Such a kernel is itself piecewise polynomial and is called a B-spline [22].

Let β^d denotes a B-spline of degree d . The B-spline of degree 0 is:

$$\beta^0(x) = \begin{cases} 1 & \text{if } |x| < 1/2; \\ 1/2 & \text{if } |x| = 1/2; \\ 0 & \text{otherwise;} \end{cases} \quad (11)$$

which is the rectangular pulse and the B-spline of higher degree are constructed by multiple convolutions of β^0 :

$$\beta^d(x) = \underbrace{\beta^0 * \dots * \beta^0}_{d+1 \text{ terms}}(x). \quad (12)$$

With this notation and considering evenly spaced samples with a step Δ , a 1D spline of degree d writes:

$$s(x) = \sum_{k \in \mathbb{Z}} c_k \beta^d((x - x_k)/\Delta). \quad (13)$$

For such 1D splines, the modeling error ϵ_f is $O(\Delta^{d+1})$ [22] [23] [18]. Hence using B-splines of higher degree decreases this error, or let one uses a coarser sampling rate for a given tolerance.

Going back to the formulation of the object representation in (2), we propose to use 3D separable B-splines of degree d as our basis functions:

$$\varphi(x, y, z) = \beta^d(x/\Delta)\beta^d(y/\Delta)\beta^d(z/\Delta), \quad (14)$$

with Δ the sampling step of the grid. Taking B-splines of degree 0 yields nothing else than the cubic voxels which are the most compact B-splines. According to the central limit theorem and B-splines being d -fold convolutions of a rectangular pulse, they become closer to a Gaussian function as their degree d increases. Thus 3D separable B-splines tend to spherically symmetric functions, while preserving a compact support of size $(d + 1)^3$. As a result, increasing the degree d not only yields an improved approximation error but also provides quasi-isotropic basis functions. These benefits are at the expense of an enlargement of the support of the basis functions and thus of an increase of the computational burden. However, as we will show, this additional cost is mitigated by the use of separable functions. The good properties of B-splines are related to the fact that they are the shortest and smoothest scaling functions for a given order of approximation [23]. More specifically, the cubic (degree 3) B-splines are members of the family of MOMS functions (Maximum Order Minimum Support), giving them a form of optimality in this context.

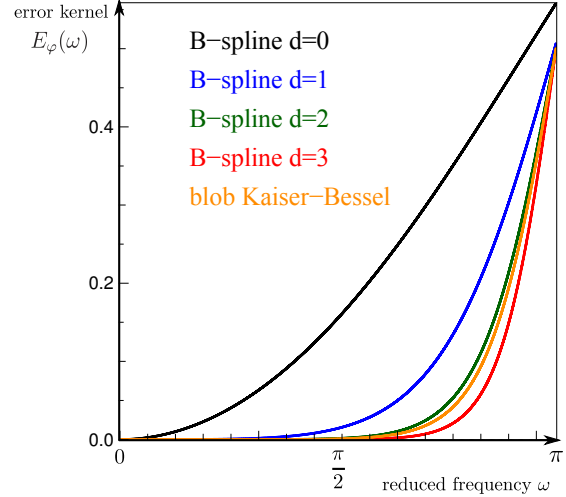


Fig. 1. Error kernels, as a function of the reduced frequency, of B-splines of different degrees d . For comparison, the error kernel of a Kaiser-Bessel blob with ideal parameters $m = 2$; $a = 2$; $\alpha = 10.4$ is plotted.

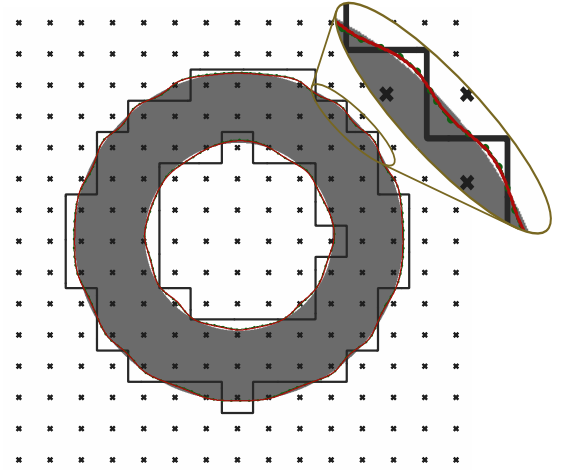


Fig. 2. Localization of the sharp edges found on thresholded approximations of a ring on a discrete 2D grid (crosses). The black frontier corresponds to the cubic voxels' representation; the green frontier with points corresponds to the blobs' representation; the red frontier corresponds to the cubic B-splines' representation. (On this figure, the green and red contours are indiscernible. See Fig. 3 to discriminate them.)

3) Comparison with the state-of-the-art basis functions:

Fig. 1 shows the error kernels (10), in 1D, for B-splines from degree $d = 0$ to 3, and for the ideal blob as defined by Matej & Lewitt [12]. The higher the degree of the B-spline, the faster the approximation error decreases below the Nyquist frequency when $\omega \times \Delta \rightarrow 0$, and tends to the optimality. Blobs also improve the quality of object modeling. We notice that the error kernel of the blob is very close to that of the quadratic B-spline (degree 2), although with a larger support.

Fig. 1 reveals that B-splines are much better basis functions for representing band-limited signals. However, modeling sharp edges, *i.e.* not band-limited signals, is one of the desired properties stated in section II-C. Indeed a typical anatomical feature of a human body in tomography is to be composed of various tissues having specific absorption levels; the object $f(x)$ to be reconstructed is therefore expected to have sharp

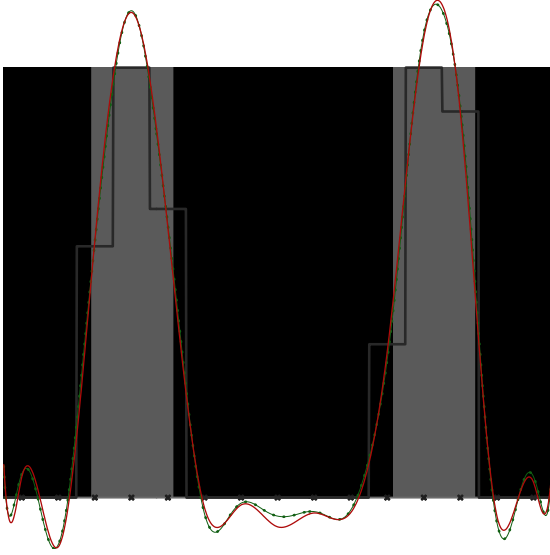


Fig. 3. 1D profile across the median horizontal line of the graph of Fig. 2. The black frontier corresponds to the cubic voxels' representation; the green frontier with points corresponds to the blobs' representation; the red frontier corresponds to the cubic B-splines' representation.

transitions between areas with different absorbing properties.

To estimate how B-splines of high degree compare to cubic voxels and blobs, we have represented the attenuation map of an absorbing ring with sharp edges on a regularly spaced 2D grid of basis functions' positions with a low resolution. The best representation, *i.e.* the model with coefficients \mathbf{c} that minimize the approximation error $\|f - \hat{f}\|$, has been computed for three different kernel functions: cubic voxel, cubic B-spline ($d = 3$) and blobs. Then each model has been interpolated on a grid much finer than the sampling grid to draw the mid-height level curve. This contour is shown by Fig. 2 for each approximation. The more accurate localization of the sharp edges by both the cubic B-spline-based and the blob-based representations is unequivocal compared with the cubic voxel-based representation which shows a staircase frontier. This behavior evidences the critical lack of isotropy of cubic voxels. Conversely, for cubic B-splines and blobs, the frontiers are precisely localized whatever the orientation. We have also calculated the root mean squared error (RMS) and the edge localization error for every approximation. These errors for cubic voxels are respectively 16.8% and 6.4%. Blobs are 1.8 times better in RMS and 6.8 times better in localization error than cubic voxels, while cubic B-splines win the contest being 1.9 times better in RMS and 8.4 times better in localization error than cubic voxels. However, as shown by Fig. 3, Gibbs oscillations appear when modeling sharp edges with basis functions having a high approximation order. Such oscillations are visible for the cubic B-spline-based and the blob-based representations. Nevertheless, these side effects are low compared with the gain of isotropy and accuracy. Moreover, a suitable choice of regularization could help flattening the oscillations.

To model the kind of objects we want to reconstruct, cubic voxels are thus not as suitable as more isotropic basis functions such as separable B-splines of higher degrees or blobs. In

principle, lowering the approximation errors of cubic voxel is possible by reducing significantly the sampling step but this would increase the computational burden and the number of parameters to manage. Compared to separable B-splines, blobs are exactly isotropic but are much more complex to handle and require more numerical operations. For instance, the computation of the sampled object f at every iteration of a regularized approach, see (4) and (8), can be computed very quickly for a B-spline based model by means of fast digital filtering operations [20], [21], [22].

B. Modeling the data

We consider a general tridimensional system (Fig. 4) where the object is static relatively to a 3D Cartesian frame with coordinates $\mathbf{x} = (x, y, z)$ evenly sampled at positions \mathbf{x}_k . We assume a flat detector and denote $\mathbf{u} = (u, v)$ the coordinates in the 2D Cartesian frame with axis aligned with the rows and the columns of the detector. Each projection is acquired with a given orientation denoted θ . The unit vector \vec{w} defines the direction perpendicular to the detector and oriented from the source S to the detector.

To improve the data model, stated in (5) and (7), we take into account detector pixel integration by defining the model for the q -th pixel at orientation θ as:

$$\begin{aligned} \tilde{y}_q^\theta &= \iint \tilde{y}^\theta(\mathbf{u}) P_q(\mathbf{u}) d^2\mathbf{u} \\ &= \sum_{k \in \Omega_q^\theta} \underbrace{\left(\iint F_k^\theta(\mathbf{u}) P_q(\mathbf{u}) d^2\mathbf{u} \right)}_{R_{qk}} c_k, \end{aligned} \quad (15)$$

where $P_q : \mathbf{u} \mapsto P_q(\mathbf{u})$ is the response of the pixel and Ω_q^θ is the set of voxels k impinging this pixel. The above approximation of true physical process dictated by the Beer-Lambert law — integration of the X-ray transform instead of the photon flux (see 1) — yields a linear model. The approximation is valid in the case of low X-ray absorption. We assume that $P_q(\mathbf{u})$ is a 2D square pulse of dimensions $\Delta_{\text{pix}} \times \Delta_{\text{pix}}$ centered at the position \mathbf{u}_q of the pixel. The pixel response is thus a separable shift-invariant function: $P_q(\mathbf{u}) = \beta^0((u - u_q)/\Delta_{\text{pix}})\beta^0((v - v_q)/\Delta_{\text{pix}})$ with β^0 given by (11).

1) *Footprint in parallel beam geometry:* In parallel beam geometry, all integration lines are aligned with $\vec{w}(\theta)$. We approximate the footprint of a voxel β_k^d by a 2D B-spline of same degree d separable along the detector axis:

$$F_k^\theta(\mathbf{u}) = \beta^d((u - u_k^\theta)/\Delta) \beta^d((v - v_k^\theta)/\Delta) \quad (16)$$

where $(u_k^\theta, v_k^\theta) = \mathbf{u}_k^\theta$ is the projection on the detector along the rays of the position \mathbf{x}_k of the k -th voxel for orientation θ . Expression (16) is exact when the direction $\vec{w}(\theta)$ of the parallel beam projection is aligned with one of the axis \vec{x} , \vec{y} , or \vec{z} ; it is only an approximation for other orientations. However the higher the degree d the better this approximation.

Thanks to the quasi-isotropy property of B-splines of sufficient degree, the footprint in our *spline driven* model (*cf.* section III-A2) has approximately the same shape whatever the orientation θ .

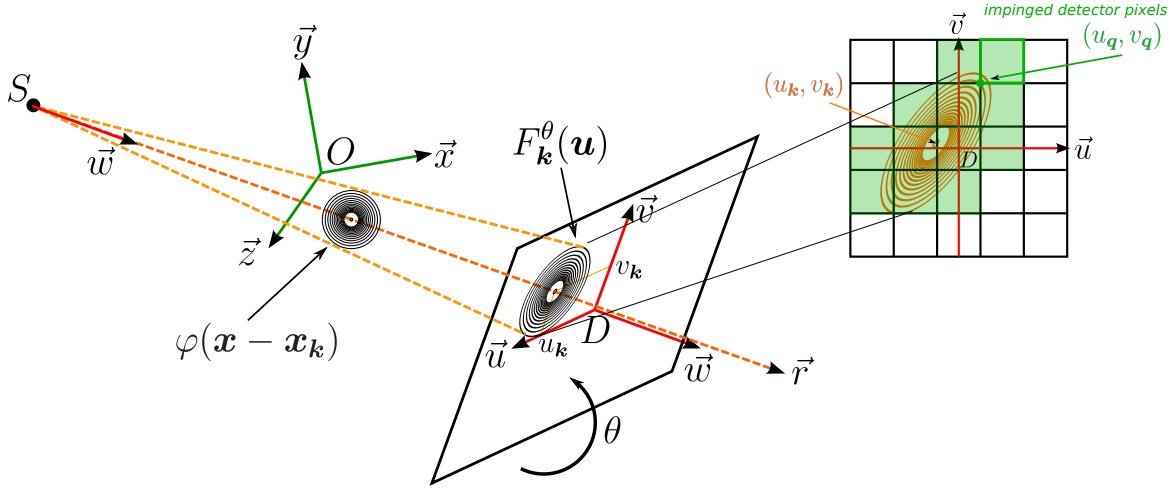


Fig. 4. Cone beam projection scheme of a basis function $\varphi(\mathbf{x} - \mathbf{x}_k)$ on the detector. θ denotes the orientation of the detector, rotating around the center O . The direction of the ray, starting from the source $S(\theta)$, orthogonal to the detector plane is identified by the vector $\vec{w}(\theta)$. The direction of the ray passing through the central position $\mathbf{x}_k = (x, y, z)$ of the k -th voxel is identified by the vector \vec{r} . The footprint of $\varphi(\mathbf{x} - \mathbf{x}_k)$ is denoted F_k^θ .

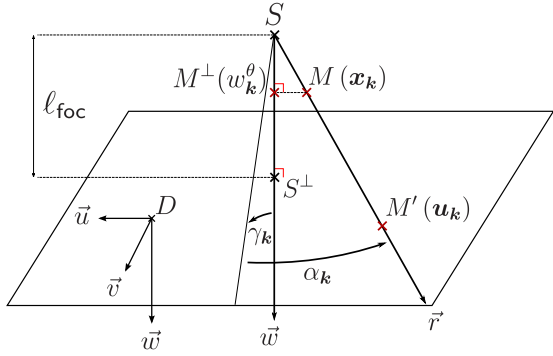


Fig. 5. Scaling parameters in cone beam geometry. ℓ_{foc} is the focal length of the system (distance between the source point S and its orthogonal projection S^\perp on the detector). $M(\mathbf{x}_k)$ is the center of the basis function β_k^d . Its cone beam projection on the detector is the point $M'(\mathbf{u}_k)$. $M^\perp(w_k^\theta)$ is the orthogonal projection of M on the straight line $\{S, \vec{w}\}$. Its position w_k is used to determine the magnification factor Γ_k^θ . α_k and γ_k are the cone beam deviation angles related respectively to directions \vec{u} and \vec{v} .

2) *Footprint in cone beam geometry*: In the case of cone beam geometry, the magnification and the distortion, both depending on the position of the voxel in the field of view, has to be taken into account (see Fig. 5). In order to keep the separability property of the footprint on the detector, we approximate these effects by scaling factors applied to the footprint in (16), such that:

$$F_k^\theta(\mathbf{u}) = \beta^d((\eta_k^\theta u - u_k^\theta)/\Delta) \beta^d((\rho_k^\theta v - v_k^\theta)/\Delta) \quad (17)$$

with (see Fig. 5):

$$\eta_k^\theta = \frac{\cos \alpha_k}{\Gamma_k^\theta}, \quad \rho_k^\theta = \frac{\cos \gamma_k}{\Gamma_k^\theta}, \quad \Gamma_k^\theta = \frac{\ell_{\text{foc}}}{w_k^\theta}, \quad (18)$$

η_k^θ and ρ_k^θ are distortion factors, Γ_k^θ is the magnification.

3) *Approximation errors of the models*: We quantified errors caused by our approximations for the footprints of our *spline driven* and compared them with the *distance driven* and *Long et al.* projectors. For a given basis function and a given model, we calculated its exact and approximated footprints.

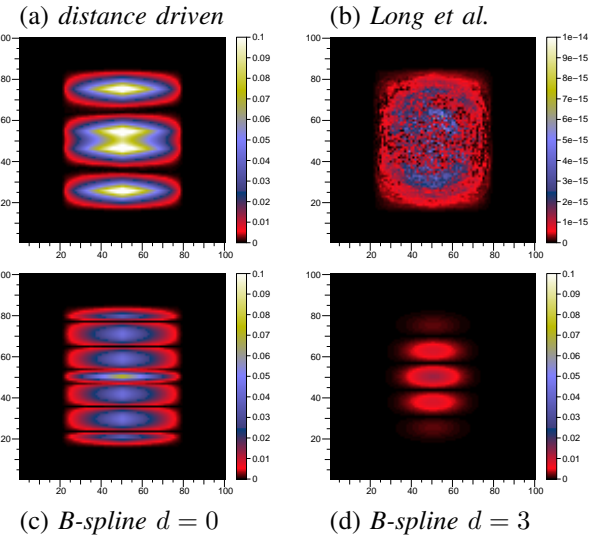


Fig. 6. Approximation errors in parallel beam geometry for footprints convolved by the pixel detector response. The projectors are: (a) *spline driven*, (b) the model of *Long et al.*, (c) and (d) our *spline driven* model. Models (a–c) are with cubic voxels, that is B-splines of degree $d = 0$; while model (d) is with B-splines of degree $d = 3$. The error maps show the absolute difference between the exact and the model-approximated footprints (assuming the same voxel shape). The detector rotates around the \vec{z} -axis. The worst case is considered here with the detector tilted by 45° with respect to the horizontal plane. Numerical values of the errors are: (a) EMAX $\simeq 12.3\%$ (maximum error) and RMS $\simeq 2.4\%$ (root mean square error); (b) EMAX $\simeq 0\%$ and RMS $\simeq 0\%$; (c) EMAX $\simeq 7\%$ and RMS $\simeq 1.3\%$; (d) EMAX $\simeq 1.3\%$ and RMS $\simeq 0.2\%$.

We considered a tomographic system with a focal length ℓ_{foc} of 949mm, a source to rotation center distance of 514mm, and a flat detector with a pixel size of $1 \times 1\text{mm}^2$. It is the same configuration as in the article of *Long et al.* [3] in the study of their own approximated footprint's errors. For the determination of the exact footprint at a given orientation of the detector, we used a Monte Carlo method consisting in calculating about 5×10^6 random lines of response (LOR) passing through the basis function. Each exact LOR was

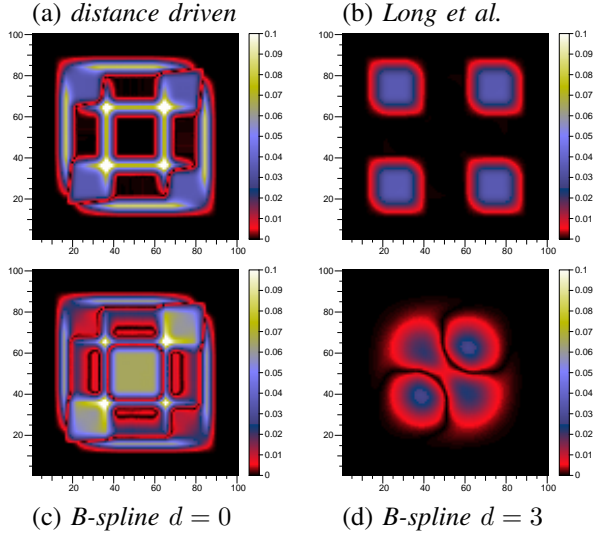


Fig. 7. Approximation errors in cone beam geometry for footprints convolved by the pixel detector response. The models are as in Fig. 6 but adapted to the cone beam geometry. The worst case is considered here: the detector is tilted by 0° with respect to the horizontal plane but the projected voxel is very off-centered (100mm, -150mm, 100mm). Numerical values of the errors are: (a) EMAX \simeq 14.5% and RMS \simeq 2.7%; (b) EMAX \simeq 3.5% and RMS \simeq 1.1%; (c) EMAX \simeq 13.5% and RMS \simeq 2.7%; (d) EMAX \simeq 2.8% and RMS \simeq 0.6%.

calculated by Romberg numerical integration [16]. The LORs approximated by each considered model were computed using their analytic expressions. Finally, we numerically computed the convolution of the footprints by the detector pixel response by summing the LOR included in the support of the pixel centered at each position of a 100×100 regular grid.

Fig. 6 displays the worst case errors caused by our approximations using B-splines with degree $d = 0$ and $d = 3$, compared with the *distance driven* and *Long et al.* approximated footprints' errors, in parallel beam geometry. Our projector proves its better accuracy, regarding *distance driven*'s approximations. As expected, in these conditions, the *Long et al.* model's approximation errors are only caused by numerical rounding errors and thus negligible.

Fig. 7 shows the same kind of approximation errors as in Fig. 6, but now in cone beam geometry. Errors are amplified due to approximations made to cope with the geometrical effects (magnification, off-axis distortions). In this configuration, *spline driven* demonstrates its better accuracy compared with both *distance driven* and *Long et al.* models, provided that the degree of the B-splines is sufficiently high.

Compared to blob-based projectors, our *spline driven* model is only approximately isotropic but requires much less numerical operations because it uses separable functions for its voxels and their footprints. In the next section we show that the computational burden of our *spline driven* model is competitive with that of more simple approaches as *distance driven*.

4) *Computational burden*: *Spline driven* increases the number of operations necessary to calculate the data values y_q^θ (15), due to the larger footprint of a given voxel. Cubic B-splines provide a good tradeoff between accuracy and computational burden. Let us give the example of a system where the voxels

and detector pixels sampling rates are approximately equal. The width of the degree d B-spline support is $s = d + 1$ in each direction. Its footprint impinges $(s + 1) \times (s + 1) = (d + 2) \times (d + 2)$ detector pixels in general. If we compare a cubic voxel ($d = 0$) with a cubic B-spline ($d = 3$), the number of impinged detector pixels for a given voxel, is only multiplied by a factor between 2 and 3 in each direction. As the footprint considered in *spline driven* is still separable, the amount of operations is multiplied by the same factor, which remains competitive. Moreover our projection scheme, as well as the cubic voxel-based approaches, is easily parallelizable, making the computational burden issue possible to address.

The next section will analyse the improvement brought by *spline driven*, applied to the iterative reconstruction process (8), when only a small number of projections are available.

IV. RESULTS ON 2D FAN BEAM RECONSTRUCTIONS

A. Reducing the number of projections

In section III-A2, we claimed that the increase of accuracy due to the use of B-splines to model the object and its projections could reduce the amount of data required for a given reconstruction quality. Figure 8 displays reconstructions of a 2D Shepp-Logan phantom with our *spline driven* model and for a variable number of fan beam projections. We considered a circular source trajectory around the object with a fixed relative position of the detector with respect to the source. The object of interest has a size of 256×256 pixels and the projections are acquired by a detector with 512 pixels. The sampling step is the same for the object and for the detector. Note that, to avoid the so-called *inverse crime* [6], [24], an exact direct model (*i.e.* with no approximation except rounding errors) was used to compute the projections for simulating the data.

The voxel coefficients \mathbf{c} were reconstructed from the set of $\{\mathbf{y}^\theta | \theta \in \Theta\}$, with Θ the set of projection angles, by minimizing the criterion (8). The data-fidelity term was:

$$\mathcal{J}_{\text{data}}(\mathbf{c}) = \sum_{\theta \in \Theta} (\tilde{\mathbf{y}}^\theta(\mathbf{c}) - \mathbf{y}^\theta)^\top \cdot (\tilde{\mathbf{y}}^\theta(\mathbf{c}) - \mathbf{y}^\theta), \quad (19)$$

In order to preserve sharp edges in the sampled object $\mathbf{f} = \Phi \cdot \mathbf{c}$, we used a relaxed total variation (TV) prior [17] for the regularization:

$$\mathcal{J}_{\text{prior}}(\mathbf{f}) = \sum_k \sqrt{\|\nabla_k \cdot \mathbf{f}\|_2^2 + \epsilon^2}, \quad (20)$$

with $\epsilon > 0$ a relaxation parameter and ∇_k a finite difference operator approximating the spatial gradient at position k . The minimization of (8) was carried out by the VMLM algorithm [15], a limited memory quasi-Newton method.

These results clearly show that the quality of the reconstruction is acceptable up to ~ 40 projections. This is an order of magnitude lower than the usual hundreds of projections required by standard reconstruction algorithms, particularly FBP. This opens the possibility to reduce of the X-ray dose delivered to the patient for data acquisition. In the following tests, we used small data sets of 60 projections.

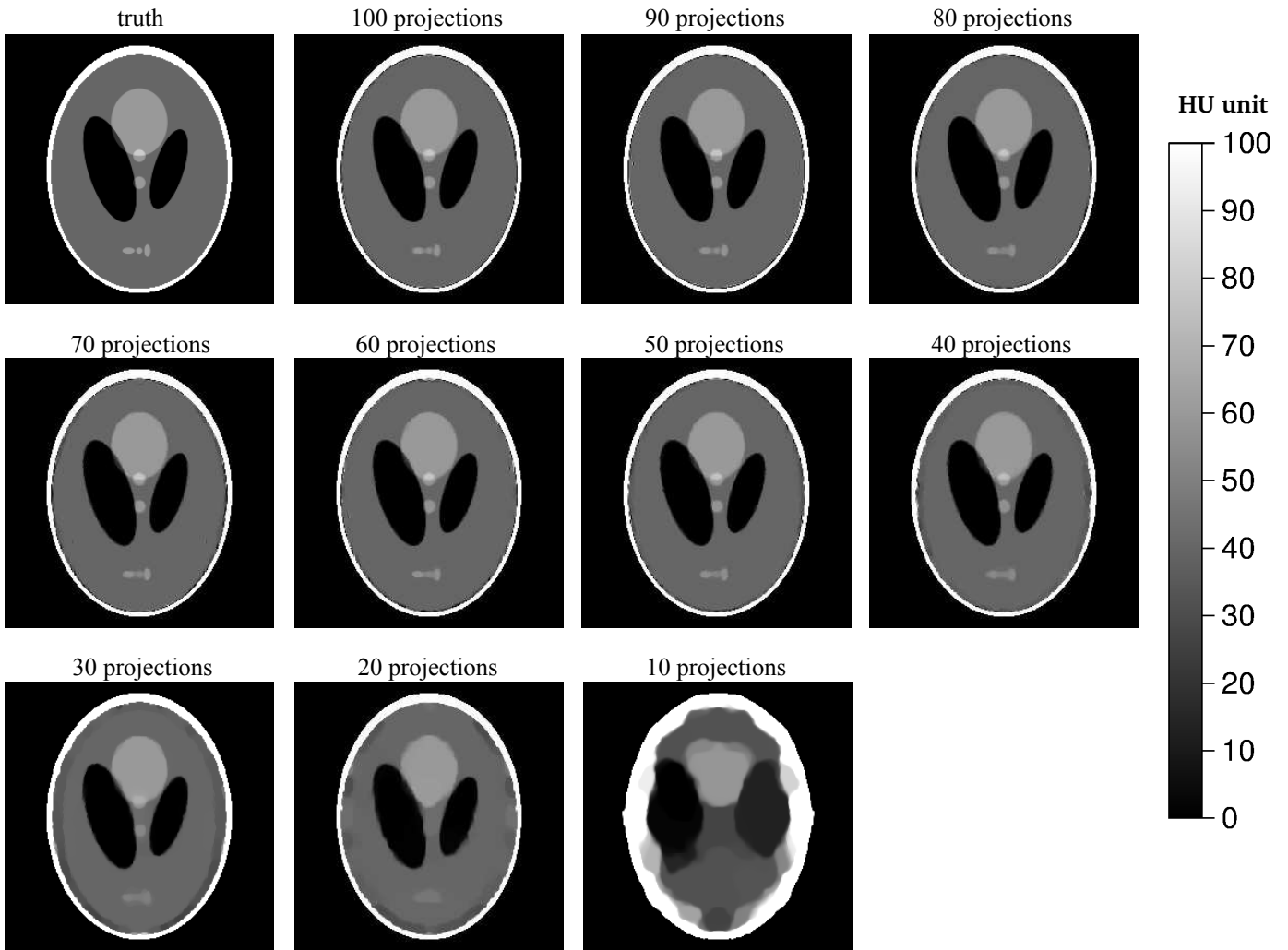


Fig. 8. Reconstructions of a 256×256 grid of a Shepp-Logan phantom with our *spline driven* projector using cubic B-splines, from a decreasing number of projections.

B. Comparison of spline and distance driven models

We compared *spline driven* and *distance driven* on simulated projections of another two-dimensional phantom (Shepp-Logan with modified values) in fan beam geometry. The system and the acquisition protocol were the same as described in section IV-A. Again, to avoid *inverse crime*, exact projections were computed for data simulation. We added to the simulated projections a non-uniform independent Gaussian noise approximately corresponding to a non-attenuated X-ray flux of 9×10^6 photons per detector pixel per projection. For the two considered models, the voxel coefficients \mathbf{c} were reconstructed from a set of 60 noisy projections $\{\mathbf{y}^\theta | \theta \in \Theta\}$, with Θ the set of projection angles, by minimizing again the criterion (8). Since the noise was independent and Gaussian, the data-fidelity term was:

$$\mathcal{J}_{\text{data}}(\mathbf{c}) = \sum_{\theta \in \Theta} (\tilde{\mathbf{y}}^\theta(\mathbf{c}) - \mathbf{y}^\theta)^\top \cdot \mathbf{W}^\theta \cdot (\tilde{\mathbf{y}}^\theta(\mathbf{c}) - \mathbf{y}^\theta), \quad (21)$$

where \mathbf{W}^θ is a diagonal weighting matrix. For the regularization, we still used the relaxed TV prior in (20).

Fig. 9 displays the reconstructions, with two magnified

regions of interest (ROI) for inspection of some details. For each projector, we use the regularization level μ which gives the best visual quality of the reconstructed object (second and third columns). With such a criterion, our model recovers most of the features without noticeable artifacts in spite of the low number of projections (60). Comparatively, *distance driven* yields some artifacts, notably in the “blue” ROI. With our model, we can consistently represent the object with a higher resolution. The bottom panels of Fig. 9 show the good isotropic behavior of the cubic B-spline basis function, at the cost of some Gibbs ripples around highly contrasted edges. This kind of artifacts could be reduced by applying the TV regularization to the finely sampled object. The optimal value μ_1 of the hyperparameter for *spline driven* is lower than the optimal value μ_2 for *distance driven* (see Fig. 10). Hence, the optimal solution with our method can extract more information from the data without noticeable artifacts. Using the same regularization weight ($\mu = \mu_1$) for the *distance driven* method (see last column of Fig. 9) yields a poorer reconstruction with many artifacts (see the purple ellipses on Fig. 9). With an optimal regularization weight, the *distance driven* method

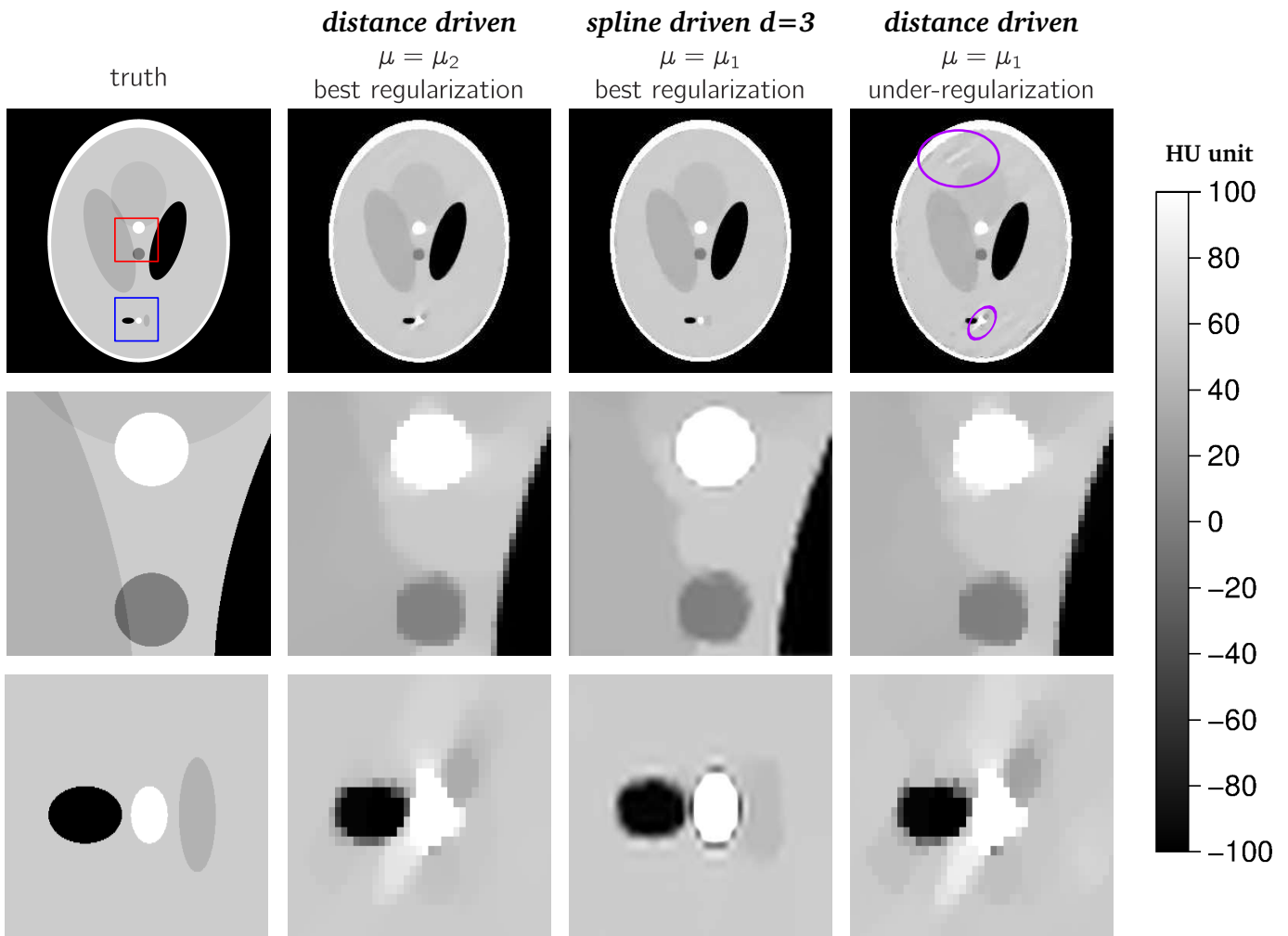


Fig. 9. Reconstructions with a 256×256 grid of a Shepp-Logan phantom, from a set of 60 fan beam projections with 512 detector pixels, with both the *spline driven* projector using cubic B-splines and the *distance driven* projector. The first column illustrates the true object. The first line shows global objects. The second and third lines respectively show a magnification on a region of interest (ROI) identified on the global true object, re-interpolated on a 8 times finer grid. The interpolant used in each reconstruction is the respective kernel function used in the projector, *i.e.* B-spline $d = 3$ for *spline driven* and cubic voxel for *distance driven*. The second column show the best reconstruction with *distance driven*. The third column corresponds to the best reconstruction with our projector *spline driven*. The fourth column is the reconstruction with *distance driven* which has used the same regularisation level as for *spline driven*, resulting in an under-regularized object.

yields a reconstruction with some distortions and a worse resolution compared to our method.

Fig. 10 shows quantitative reconstruction results. The curves present the evolution of the RMS error in the two ROIs (a given color corresponds to a given ROI), as a function of the hyperparameter μ , for the reconstructed objects. First, each curve appears to be convex; thus the best reconstruction in each ROI is obtained for a unique optimal value of μ . Visual assessment (see Fig. 9) confirms that the RMS error computed in well chosen regions of interest is an appropriate metric to evaluate the quality of a reconstructed object, because they match quite well the empirical values found in Fig. 9. Second, for each ROI, the *spline driven*'s RMS is always lower than the *distance driven*'s RMS. Thus according to this error metric, our projector quantitatively yields the best performances.

V. CONCLUSIONS

This paper described our *spline driven* model for iterative reconstruction in X-ray CT, whose preliminary results have been previously published in a conference [13]. Our motivation was to achieve a good compromise between the accuracy of the tomographic projection model while keeping the computational burden as low as possible. By exploiting a more accurate direct model compared to current models such as the *distance driven* one, we expected to enhance the quality of the restored object and to reduce the minimal amount of tomographic data required for an interpretable reconstruction. Thus, not only the diagnosis can be improved but the dose of radiation received by the patient can also be reduced. In tomography, only regularized inverse methods provide optimal reconstructions but lead to iterative algorithms. This is why we wanted to develop a fast projection model.

Our approach uses the good properties of B-spline basis functions to model the object of interest and also to

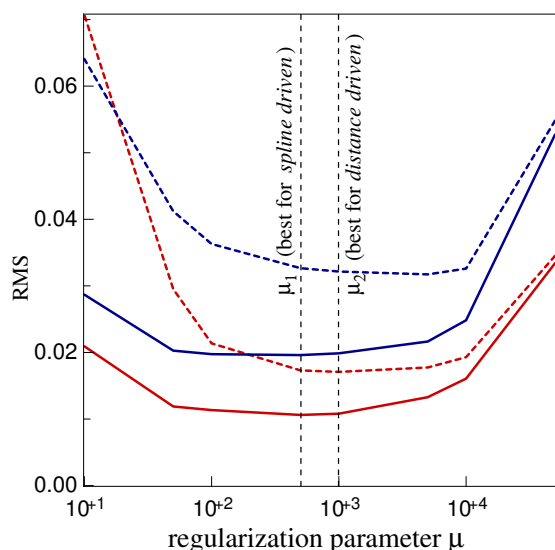


Fig. 10. Root mean squared error in the two ROIs (see Fig. 9) of the reconstructed object, normalized by the maximum value in the ROI, for various values of the hyperparameter μ (logarithmic scale). The solid curves correspond to reconstructions with the *spline driven* projector, and the dashed curves correspond to reconstructions with the *distance driven* projector. Symbols pointing the empirical values of the hyperparameter μ used in the reconstructions of Fig. 9 are plotted on the curves.

approximate its projections and, possibly, account for pixel integration. Using separable 3D B-spline basis functions with a sufficiently high level, our model of the object is nearly isotropic which is a clear improvement compared to models based on cubic voxels. We also introduce a separable 2D B-spline based approximation to compute the projection of our voxels on the detector for various (parallel, fan beam and cone beam) beam geometries. Our model is not as good as blobs which are exactly isotropic but, being separable and using more compact basis functions, it is much faster to compute than a blob-based model. The computational burden of our model is similar to that of the *distance driven* or the Long *et al.* [3] models. Compared to these models and using a similar cubic voxel (which is not what we advocate to use with our approach), our projection model is more accurate than the *distance driven* one whatever the type of projection. With cubic voxels, the Long *et al.* [3] model remains the most accurate in non-parallel beam geometry (the Long *et al.* model is exact in parallel beam geometry). This is not true anymore if we use B-splines of higher degree, for which our *spline driven* model becomes the best model. In our opinion, a good compromise between accuracy and speed is to use cubic B-splines.

We also studied the benefit of an improved model like ours when it is implemented in an iterative regularized reconstruction method. By varying the number of available measurements, we have shown that it is possible to obtain reliable reconstructions with only 50-60 projections which is much fewer than the ~ 500 projections needed by analytic methods such as FBP. Note that, to avoid *inverse crime*, we used an exact numerical projection to simulate the data (*i.e.* not the direct model used for the reconstruction). On a limited

number of 60 projections, using our model yields substantial gain in object quality compared with reconstructions using the *distance driven* projector. Qualitatively, there are less artifacts and more reliable features are visible; quantitatively, the RMS error is lower. Moreover, to achieve the best reconstructions (for a given projection model), the relative weight of the priors is lower with our model which means that reconstruction methods with coarser models must regularize more and thus do not thoroughly exploit the information in the data.

The tests presented here were based on simulated projections. In a companion paper currently under peer reviewing [14], we exploit our model to produce 3D and 3D+*t* (spatio-temporal) reconstructions on both simulated and empirical data. In the 3D+*t* case, the ability to achieve acceptable reconstructions from a much reduced number of projections is a strong requirement. Indeed, in practice, the object of interest is approximately the same only for a very limited number of observations.

REFERENCES

- [1] B. DeMan and S. Basu. *Distance driven projection and backprojection in three dimensions*. Physics in Medicine and Biology, 2004.
- [2] J.A. Fessler. *Iterative methods for image reconstruction*. IEEE International Symposium on Biomedical Imaging Tutorial, Arlington Virginia, 2006.
- [3] Y. Long, J.A. Fessler and J.M. Balter. *3D Forward and Back-Projection for X-Ray CT Using Separable Footprints*. IEEE Transactions on Medical Imaging, 2010.
- [4] S. Horbelt, M. Liebling and M. Unser. *Discretization of the Radon transform and of its inverse by spline convolutions*. IEEE Transactions on medical imaging, 2002.
- [5] P.M. Joseph. *An improved algorithm for reprojecting rays through pixel images*. IEEE Transactions on Medical Imaging, 1982.
- [6] J. Kaipio and E. Somersalo. *Statistical inverse problems: discretization, model reduction and inverse crimes*. Journal of Computational and Applied Mathematics, 2007.
- [7] M. Slaney and A. Kak. *Principles of computerized tomographic imaging*. SIAM, Philadelphia, 1988.
- [8] R.M. Lewitt. *Multidimensional digital image representations using generalized Kaiser-Bessel window functions*. JOSA A, 1990.
- [9] R.M. Lewitt. *Alternatives to voxels for image representation in iterative reconstruction algorithms*. Physics in Medicine and Biology, 1992.
- [10] S. Matej and R.M. Lewitt. *Image representation and tomographic reconstruction using spherically symmetric volume elements*. IEEE Transactions on Medical Imaging, 1993.
- [11] S. Matej and R.M. Lewitt. *Efficient 3D grids for image reconstruction using spherically-symmetric volume elements*. IEEE Transactions on Medical Imaging, 1995.
- [12] S. Matej and R.M. Lewitt. *Practical considerations for 3D image reconstruction using spherically symmetric volume elements*. IEEE Transactions on Medical Imaging, 1996.
- [13] F. Momey, L. Denis, C. Burnier, É. Thiébaud, J.-M. Becker and L. Desbat *A new representation and projection model for tomography, based on separable B-splines*. IEEE Nuclear Science Symposium and Medical Imaging Conference, 2011.
- [14] F. Momey, É. Thiébaud, C. Burnier, L. Denis, J.-M. Becker and L. Desbat *Regularized reconstruction for dynamic X-ray CT without motion compensation*. Manuscript in preparation, 2014.
- [15] J. Nocedal. *Updating quasi-Newton matrices with limited storage*. Mathematics of computation, 1980.
- [16] W. Romberg *Vereinfachte numerische integration* Norske Vid. Selsk. Forh.(Trondheim), 1955.
- [17] L.I. Rudin, S. Osher and E. Fatemi. *Nonlinear total variation based noise removal algorithms*. Physica D: Nonlinear Phenomena, 1992.
- [18] P. Thévenaz, T. Blu and M. Unser. *Interpolation Revisited*. IEEE Transactions on Medical Imaging, 2000.
- [19] É. Thiébaud, *Introduction to Image Reconstruction and Inverse Problems*, in *Optics in Astrophysics*, R. Foy & F.-C. Foy (Eds.), NATO ASI Series **198**, pp. 397-422 Springer (Amsterdam), 2005.

- [20] M. Unser, A. Aldroubi and M. Eden. *B-spline signal processing: Part I-Theory*. IEEE Transactions on Signal Processing, 1993.
- [21] M. Unser, A. Aldroubi and M. Eden. *B-spline signal processing: Part II-Efficient design and applications*. IEEE Transactions on Signal Processing, 1993.
- [22] M. Unser. *Splines: A perfect fit for signal and image processing*. IEEE Signal Processing Mag., 1999.
- [23] M. Unser. *Sampling-50 years after Shannon*. Proceedings of the IEEE, 2000.
- [24] A. Wirgin *The inverse crime* arXiv Mathematical Physics, 2004.
- [25] A. Ziegler, T. Köhler, T. Nielsen and R. Proksa. *Efficient projection and backprojection scheme for spherically symmetric basis functions in divergent beam geometry* Medical Physics, 2006.